ADVANCED MATERIALS
www.advmat.de

Tunable Interlayer Interactions in Exfoliated 2D van der Waals Framework $Fe(SCN)_2(Pyrazine)_2$

Jacob McKenzie, Doran L. Pennington, Thomas Ericson, Elana Cope, Aaron J. Kaufman, Anthony F. Cozzolino, David C. Johnson, Kentaro Kadota, Christopher H. Hendon,* and Carl K. Brozek**

2D materials can be isolated as monolayer sheets when interlayer interactions involve weak van der Waals forces. These atomically thin structures enable novel topological physics and open chemical questions of how to tune the structure and properties of the sheets while maintaining them as isolated monolayers. Here, this work investigates 2D electroactive sheets that exfoliate in solution into colloidal nanosheets, but aggregate upon oxidation, giving rise to tunable interlayer charge transfer absorption and photoluminescence. This optical behavior resembles interlayer excitons, now intensely studied due to their long-lived emission, but which remain difficult to tune through synthetic chemistry. Instead, the interlayer excitons of these framework sheets can be modulated through control of solvent, electrolyte, oxidation state, and the composition of the framework building blocks. Compared to other 2D materials, these framework sheets display the largest known interlayer binding strengths, attributable to specific orbital interactions between the sheets, and among the longest interlayer exciton lifetimes. Taken together, this study provides a microscopic basis for manipulating long-range opto-electronic behavior in van der Waals materials through molecular synthetic chemistry.

1. Introduction

Graphene, CrI_3, and other layered compounds derive their unique properties from weak interlayer van der Waals interactions that allow them to exist as atomically thin sheets. These 2D van der Waals (vdW) materials display distinct quantum mechanical behavior that finds use in a range of technologies including batteries,[1,2] catalysts,[3,4] superconductors,[5,6] topological insulators,[7] and photovoltaic devices.[8] However, strong interlayer interactions can also dominate the behavior of 2D vdW materials. For example, whereas monolayers of black phosphorous possess an optical band gap of 1.55 eV, the gap decreases to 1.05 eV for dimers and to just 0.46 eV for bulk.[9] In addition, the already-high charge mobility of 286 $cm^2\ V^{-1}\ s^{-1}$ of black phosphorous when prepared as several stacked layers increases to 1000 $cm^2\ V^{-1}\ s^{-1}$ simply by increasing the film thickness.[10] Similar layer-dependent phenomena manifest in structurally similar tellurene (2D elemental Te) and GeP_3 or SnP_3, along with certain metal chalcogenides including InSe, TiS_2, SnS, and the group-10 family (e.g., PtS_2 or $PtTe_2$).[11–17] On the other hand, the group-6 and group-7 transition metal dichalcogenides (e.g., WSe_2 and MoS_2) and ReS_2, display layer-dependent optical gaps, but the effect is much less extreme.[16] This marked difference in interlayer interactions has been correlated with interlayer binding strengths, which range from 23 meV $Å^{-2}$ for weakly interacting graphene, 33 meV $Å^{-2}$ for strongly interacting black phosphorous, and 92 meV $Å^{-2}$ for interactions that are better described as "bond-like" for GeP_3.[17,18] Microscopically, interactions between electron lone pairs in the so-called van der Waals gap between these layered compounds has been proposed as the origin of strong interlayer interactions. In fact, X-ray scattering measurements have detected electron density between TiS_2 sheets resembling S-S bonding interactions.[19] Beyond single-compound materials, interlayer interactions influence heterostructures as well. Practically, exciton annihilation rates in MoS_2 and WS_2 can be reduced by one-to-two orders of magnitude by using an Al_2O_3 or $SrTiO_3$ substrate as opposed to a quartz substrate.[20] Furthermore, band-edge offsets in heterojunctions such as $MoSe_2/WSe_2$ lead to interlayer excitons[21] with long recombination lifetimes and ultra-high charge carrier/thermal transport due to efficient polaron delocalization across layers.[22] As a result, interlayer excitons find utility in advanced field-effect transistors,[23,24] photodetectors,[25,26] and quantum emitters.[27] Despite the importance of interlayer interactions in tuning 2D vdW behavior, little is known about their chemistry, in part

J. McKenzie, D. L. Pennington, E. Cope, A. J. Kaufman, D. C. Johnson, K. Kadota, C. H. Hendon, C. K. Brozek
Department of Chemistry and Biochemistry
Materials Science Institute
University of Oregon
Eugene, OR 97403, USA
E-mail: kadota.kentaro.7a@kyoto-u.ac.jp; chendon@uoregon.edu; cbrozek@uoregon.edu
T. Ericson, A. F. Cozzolino
Department of Chemistry and Biochemistry
Texas Tech University
Lubbock, TX 79409, USA

The ORCID identification number(s) for the author(s) of this article can be found under https://doi.org/10.1002/adma.202409959

DOI: 10.1002/adma.202409959

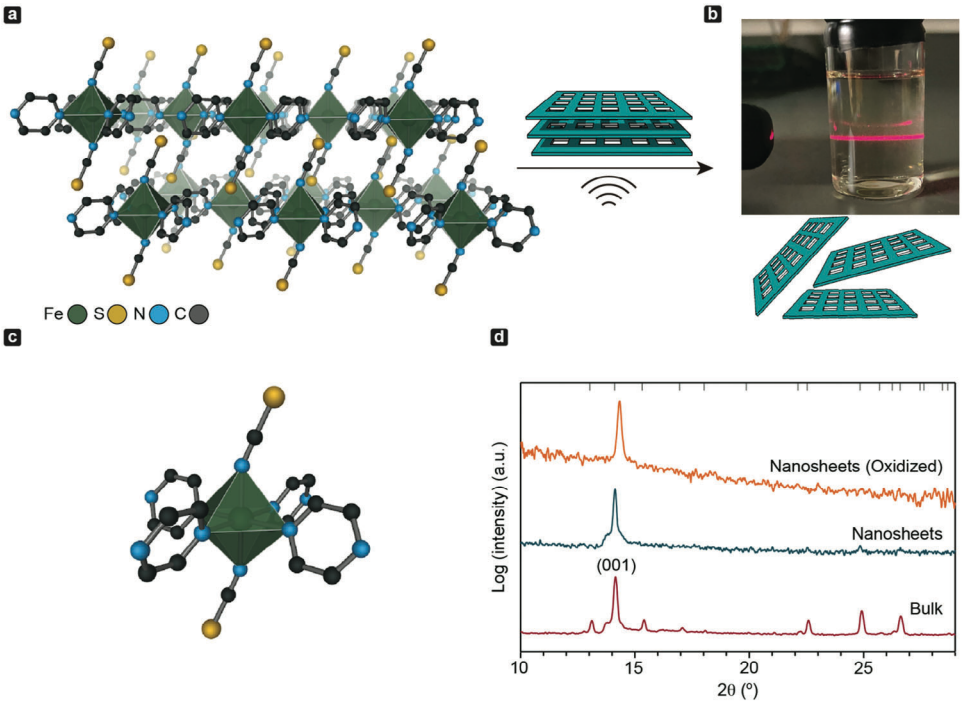

Figure 1. a) 3D crystalline structure for $Fe(SCN)_2(pyz)_2$. (For clarity, 2 layers are shown) b) methanolic solution of exfoliated $Fe(SCN)_2(pyz)_2$ displaying the Tyndall effect. c) local octahedral coordination environment of iron centers. d) Powder X-ray diffraction patterns for the bulk and exfoliated 2D sheets pre and post atmospheric oxidation.

due to the limited set of materials and synthetic methods for investigating them.

Here, we report a combined experimental-computational investigation into the tunable interlayer interactions of the 2D metal-organic framework (MOF) $Fe(SCN)_2(pyrazine)_2$. These 2D materials exfoliate under sonication to yield a colorless solution of colloidally stable nanosheets with Fe in the 2+ oxidation state. Upon chemical or electrochemical oxidation, however, an intense and broad absorption band emerges. DFT calculations indicate that oxidation creates mixtures of Fe^{3+}/Fe^{2+} sheets that interact with an anomalously large binding strength of ≈64 meV $Å^{-2}$ Simulations also suggest that this absorption band arises from interlayer charge transfer from the S atom of an Fe^{3+}-SCN fragment to a pyrazine ring in the adjacent layer across the vdW gap. Although this excitation resembles interlayer excitons, it occurs between layers of the same material rather than between heterodimers. Whereas interlayer excitons and binding strengths remain difficult to tune in conventional vdW materials,[28] the 2D vdW MOF is amenable to a range of chemical modification strategies. Experimentally, this interlayer charge transfer band modulates in response to solvents of varying dielectric strengths that screen the interlayer interaction, to electrolyte that separate the sheets, and in response to changes in the chemical composition of the donor-acceptor components of the 2D MOF. Taken together, these results expand the range of interlayer interactions through synthetic tunability, while inching their orbital nature closer toward true covalent binding.

2. Results and Discussion

In search of vdW materials with wide synthetic tunability, we targeted a subset of MOF structures due to their diverse compositions. Although most MOFs behave as electronic insulators, a growing family of atomically thin structures exhibit the semiconducting or metallic behavior expected for vdW materials with strong interlayer interactions.[29] Indeed, recent reports indicate that charge mobility between sheets may exceed mobility within a 2D sheet.[30] However, studies of interlayer interactions between 2D MOFs remains largely limited to the "graphitic," honeycomb-type structures dominated primarily by π–π forces akin to graphene.[31] Inspired by the ability of the lone pairs in black phosphorous or TiS_2 to interact across the vdW gap, we targeted the 2D layered MOF $Fe(SCN)_2(pyrazine)_2$ (Fe-SCN-pyz, **Figure 1**a,c), which features axial SCN^- groups and their lone pairs oriented toward adjacent sheets. We hypothesized that in a similar manner to the lone pairs of black phosphorus, the SCN^- groups would mediate vdW interactions and increase the accessible contact area between sheets. Similar pyrazine-bridged materials have exhibited semiconductor behavior.[32] Fe-SCN-pyz was prepared according to reported synthetic procedures[33] and the isolated microcrystalline powder was analyzed by powder X-ray diffraction (PXRD), showing the expected Bragg reflections for a layered structure (Figure 1d). To generate isolated 2D sheets, the bright orange microcrystalline powder was exfoliated via ultrasonication in methanol to yield an optically clear yellow solution that displayed the Tyndall effect (Figure 1b). In addition to

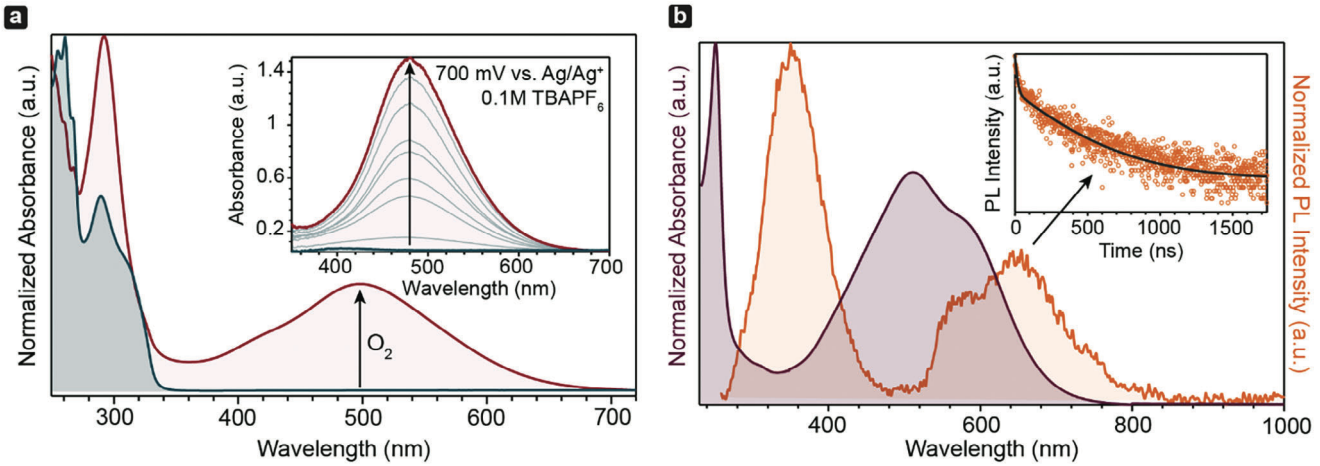

Figure 2. a) UV–vis spectrum of exfoliated Fe-SCN-pyz nanosheets suspended in MeCN pre and post atmospheric oxidation. Inset shows UV–vis spectrum of exfoliated Fe-SCN-pyz nanosheets suspended in a 0.1-M $TBAPF_6$ MeCN solution as 700mV vs Ag/Ag^+ is applied with a platinum mesh working electrode, platinum wire counter electrode, and silver wire pseudoreference. b) UV–vis spectra and photoluminescence spectra of the air oxidized Fe-SCN-pyz nanosheets suspended in DCM after excitation at 250 nm. Inset shows photolumiscence decay for the interlayer emission, with a biexponential fit.

methanol, the material readily suspended in a variety of both polar and nonpolar solvents (Figure S3, Supporting Information). To confirm sample stability to exfoliation, this nanosheet suspension was dried to yield a light orange powder and analyzed again by PXRD, confirming retention of crystallinity, with strong preferential orientation along the (001) crystallographic plane. AFM measurements show aggregated nanosheets as expected from the drying process. Nevertheless, many of these agglomerates were only 1–5 nm thick (Figure S10, Supporting Information). Because simulated crystal structure of a monolayer is ≈1 nm thick, these AFM measurements indicate the presence of monolayers and aggregates as thin as 5 layers.

As a powder under aerobic conditions, Fe-SCN-pyz remains bright orange indefinitely, while as a methanolic suspension it progressively darkens from yellow to violet over the course of 2 weeks. The violet-colored solution still displays the Tyndall effect, however, suggesting the sheets remain separated. When dried, this nanosheet suspension yields a dark purple, nearly black powder. The crystallinity of this material is preserved with preferential orientation along the (001) crystallographic plane and a slight shift of the (001) reflection indicating a relative contraction of interlayer spacing in the crystal lattice (Figure 1d). In addition, high resolution TEM images support the preservation of nanosheet structure after excessive air exposure (Figure S9, Supporting Information).

To investigate this stark color change, the samples were measured by solution-state spectroscopy. **Figure 2**a displays UV–vis spectra of nanosheets suspended in MeCN under anerobic conditions and after atmospheric exposure. Both samples show prominent features in the UV region, similar to the reported absorption spectrum of the analogous material Co-SCN-pyz.[34] Most notably, upon air exposure, a broad and intense absorption band emerges between 360 and 700 nm. The intensity of the band is consistent with an allowed electronic transition, while its breadth suggests vibronic coupling and its energetic position indicates it involves states below the optical band gap – all characteristics of intersheet charge transfer excitons.[35–38] Indeed, photoluminescence (PL) measurements of the oxidized nanosheets suspended in dichloromethane and excited with 250-nm light reveal two emission profiles (Figure 2b). The PL bands centered at ≈340 nm resemble the intralayer charge recombination observed in the analogous Co-SCN-pyz,[34] while an additional PL features appears at ≈660 nm. Secondary emission features often are seen in 2D materials with strong interlayer coupling that enables charge transfer across the vdW gap. Hence, we assign the PL band at ≈660 nm to the charge recombination of an interlayer exciton.[39–44] We propose that excitation with 250-nm light promotes a π-to-π^* transition within the pyrazine rings, giving rise to intralayer emission at ≈340 nm, whereas the interlayer emission at ≈660 nm occurs following hole transfer across the vdW gap from pyrazine to a pendant SCN^-. Whereas many studies have documented interlayer excitons in solid-state samples, few if any have been observed for suspended solutions due to the spatial separation of dissolved species. Here, we propose interlayer excitons emerge in suspended 2D sheets due to aggregation upon oxidation.

Interlayer excitons are often distinguished from intralayer excitons by their longer fluorescence lifetimes induced by decreased electron-hole wavefunction overlap.[45] The inset in Figure 2b shows the time-resolved photoluminescence of the interlayer emission process fitted to a biexponential decay: $I(t) = B_1 e^{-t/\tau_{slow}} + B_2 e^{-t/\tau_{fast}}$. The fit produces τ_{slow} and τ_{fast} lifetimes of 400 and 15 ns, respectively, both longer than the intralayer emission (≈1 ns) seen in the full-time-resolved photoluminescence decay (Figure S7, Supporting Information). The lifetimes of interlayer excitons in vdW materials are often 1–100 ns and, in rare cases, microseconds. In such instances, the exciton is described as either a dark exciton, resulting from an indirect transition[46] or as a Moiré trapped exciton induced by lattice mismatches in 2D heterostructures.[47,48] Dark excitons often display broadened excitonic absorption profiles and as additional low-intensity, red-shifted absorption features.[37] Tentatively, we assign the

secondary feature to a dark exciton of its broad absorption profile and because it is redshifted from a secondary, presumably "bright exciton" when suspended in dichloromethane.[37] Interestingly, we also observe evidence of Moiré fringes in the TEM images of air-oxidized nanosheets (Figure S9, Supporting Information), as a result of differing lattice parameters between Fe^{2+}-SCN-pyz and $Fe^{2+/3+}$-SCN-pyz.

To understand the effect of air on the Fe-SCN-pyz oxidation state and the formation of the interlayer excitonic band, the samples were studied by ^{57}Fe Mössbauer spectroscopy. In contrast to the high-spin Fe^{2+} observed for freshly prepared powder of Fe-SCN-pyz, ^{57}Fe Mössbauer spectra of nanosheets suspended in MeOH and exposed to air for 2 months display two distinct doublets. The isomer shift at 1.11 mm s^{-1} with a large quadrupolar splitting of 3.36 mm s^{-1} is assignable to high-spin Fe^{2+}. The second doublet has a decreased isomer shift of 1.02 mm s^{-1} and quadrupolar splitting of 2.09 mm s^{-1} consistent with high-spin Fe^{3+} (Figure S14, Supporting Information). Interestingly, even with excessive atmospheric oxidation, the material equilibrates to a mixed-valent state with 21% Fe^{2+} and 79% Fe^{3+}. Further evidence of mixed valency was confirmed by diffuse-reflectance UV–vis spectra of air-oxidized powder, which displayed a broad band in the near IR characteristic of an intervalence charge transfer (IVCT) between Fe^{2+}-Fe^{3+} (Figure S5, Supporting Information). Atmospheric oxidation is further confirmed by the presence of a coordinated OH^- stretch in the Fourier-transform infrared spectra of the air- exposed sample at 3400 cm^{-1} (Figure S17, Supporting Information). The hydroxide is both a byproduct of O_2 reduction and the charge-compensating anion to the mixed valent $Fe^{2+/3+}$-SCN-pyz structure.

To further understand the interplay between Fe oxidation state and visible light absorption, voltammetric spectroelectrochemistry was performed on a solution of nanosheets suspended in MeCN under anaerobic conditions. The electrochemical cell consisted of a quartz cuvette with a platinum mesh working electrode, platinum wire counter electrode, silver wire pseudo reference electrode, and 0.1-M $TBAPF_6$ as the supporting electrolyte. Cyclic voltammetry measurements of the suspended nanosheets revealed a reversible redox feature centered at 400 mV versus Ag that is assignable to the $Fe^{2+/3+}$ redox couple (Figure S11, Supporting Information). To this solution, a constant 700 mV potential was applied while UV–vis spectra were recorded in 2-minute intervals. The inset in Figure 2a displays the growth of an absorption feature at ≈500 nm during the application of the oxidizing potential. The reversibility of this ≈500 nm feature was explored by applying a 100 mV reducing potential after oxidation, causing the feature to fully bleach. Finally, 700 mV was applied once more and the ≈500 nm feature returned (Figure S12, Supporting Information).

To identify the underlying mechanism driving optical absorption in solutions of oxidized nanosheets, a series of DFT calculations were performed on monolayer and bulk systems to model the behavior of the material with and without interlayer interactions. First, we obtained the interlayer coupling strength, defined as the energy needed to separate the layered material into individual sheets an infinite distance apart, as a function of Fe oxidation. The fully reduced Fe^{2+} bulk material yields an interlayer binding energy of 2 meV $Å^{-2}$, which is far weaker than the known vdW materials and supports the experimental finding that ultrasonication readily exfoliates the solid material to yield a suspension of nanosheets. However, when the bulk model system is oxidized to 50% Fe^{3+}, the interlayer spacing contracts by 0.8 Å which is accommodated by axial SCN^- of one layer intercalating within the open square pores of the next layer formed by the pyrazine units (**Figure 3a**). This contraction is likely encouraged by enhanced electrostatic attraction between the electron-rich S atom of isothiocyanate and Lewis-acidic Fe^{3+} sites, as the Fe-S distance contracts from 4.68 to 4.44 Å upon oxidation. Aside from compression in the stacking direction, no significant structural rearrangements occur when the material oxidizes. In this contracted, oxidized structure, the interlayer coupling energy increases to 64 meV $Å^{-2}$ This is among the largest interlayer coupling strengths ever reported, and is nearly double the calculated coupling energy of black phosphorous.[49] Furthermore, this demonstrates for the first time the utility of redox in modulating the coupling strength for a material of fixed composition. Additionally, this result suggests that nanosheets are likely to experience a strong energetic push to aggregate in solution to some extent when oxidation occurs, as the sheets are significantly stabilized by interlayer interactions in the mixed-valent state (Figure 3a).

Using both the fully reduced and the mixed-valent models, the optical properties of the sheets as both monolayers and as bulk systems with interlayer interactions were computed using a range-dependent model dielectric function to describe the screened Coulomb potential of the excited state. The gold standard for these calculations, GW-BSE, is too computationally expensive for this system which contains 216 atoms and ≈780 valence electrons. Instead, the exchange-correlation kernel can provide an approximation of the screened Coulomb potential, avoiding a costly ab initio calculation. The solutions to the Casida eigenvalue equation that result from this approach, similarly to the solutions of the Bethe-Salpeter equation in GW-BSE, have been shown to accurately recover optical properties in a number of systems, including in van der Waals materials.[50–55] Under this TD-DFT scheme, range-dependent hybrid functionals such as HSE06 can be used, but the PBEsol exchange-correlation kernel was preserved for this model. The precedent of this approach for a range of materials, along with the recovery of the most intense visible absorption to within 5 nm of the experimental value for this study, assures that the chosen model is sufficiently accurate to describe the observed optical properties of this material. The fully reduced Fe^{2+} material, both as an isolated monolayer and as an aggregated bulk model, features intense absorption between 225 and 350 nm, corresponding to the experimentally assigned pyrazine and SCN^- transitions. In both structural arrangements, any visible absorption is negligible. Similarly, the isolated monolayer of the mixed-valent material only displays significant absorption in the UV range. However, in an aggregated arrangement of the mixed-valent material an intense and broad visible absorption peaking at 510 nm is observed (Figure 3b). Examination of the wavefunctions associated with the strongest-absorbing excitation reveals an intersheet transition from a donor level centered on the S atom of SCN^- from one layer into the surrounding pyrazine units bonded to the next layer (Figure 3c). Because interlayer aggregation is necessary to bring pyrazine into proximity to the interdigitated SCN^-, this transition appears only in the layered material after oxidation-induced contraction. Indeed, the distance between the S atom of

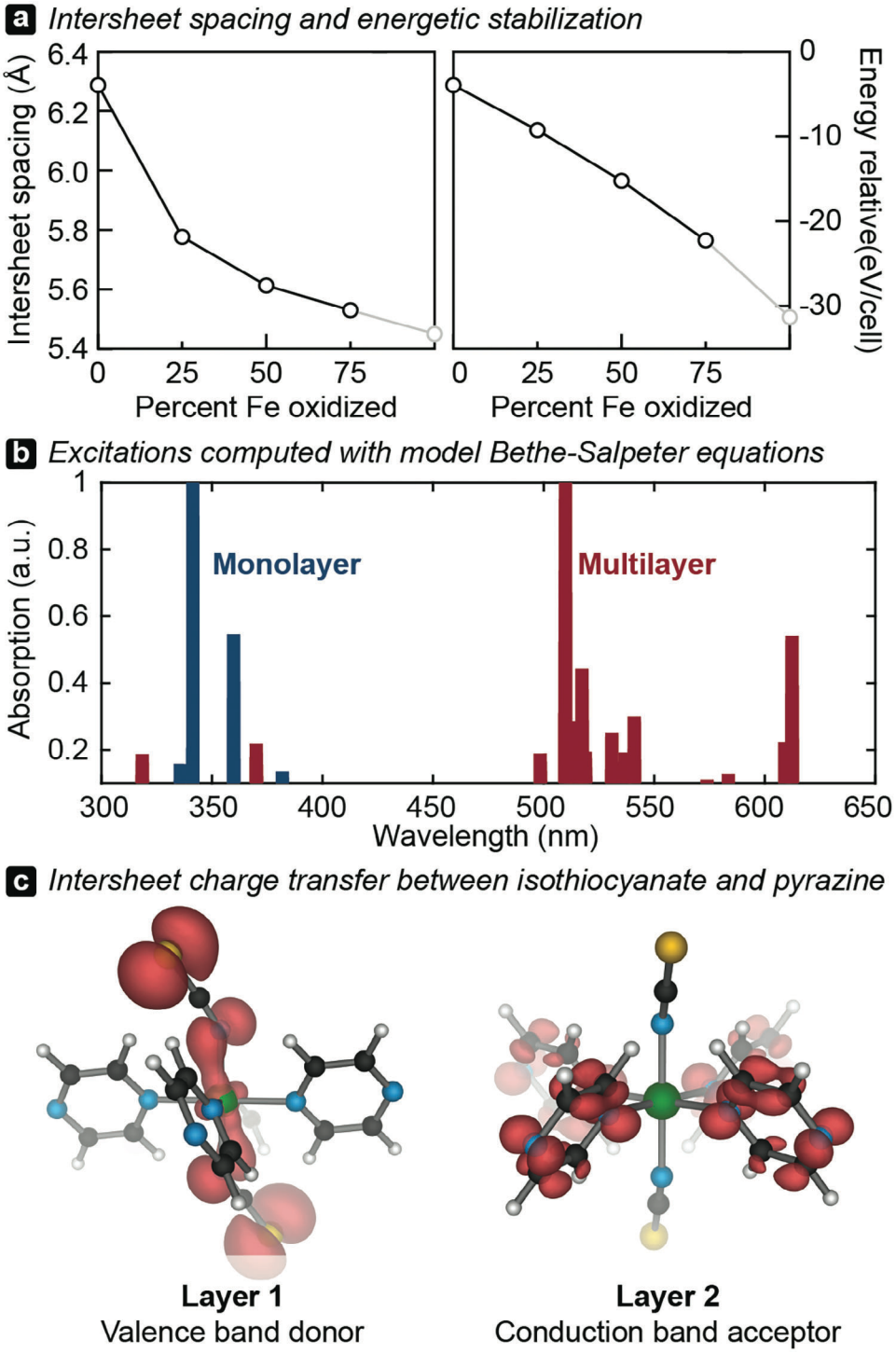

Figure 3. a) Owing to intersheet exchange interactions, the mixed valent sheets exhibit increased vdW stabilization compared to the fully reduced system. b) Simulated transitions and relative absorption strength for monolayer and bulk mixed valent 1:1 Fe^{2+}:Fe^{3+}-SCN-pyz. c) The transition at 510 nm involves transitions between the depicted occupied and virtual bands.

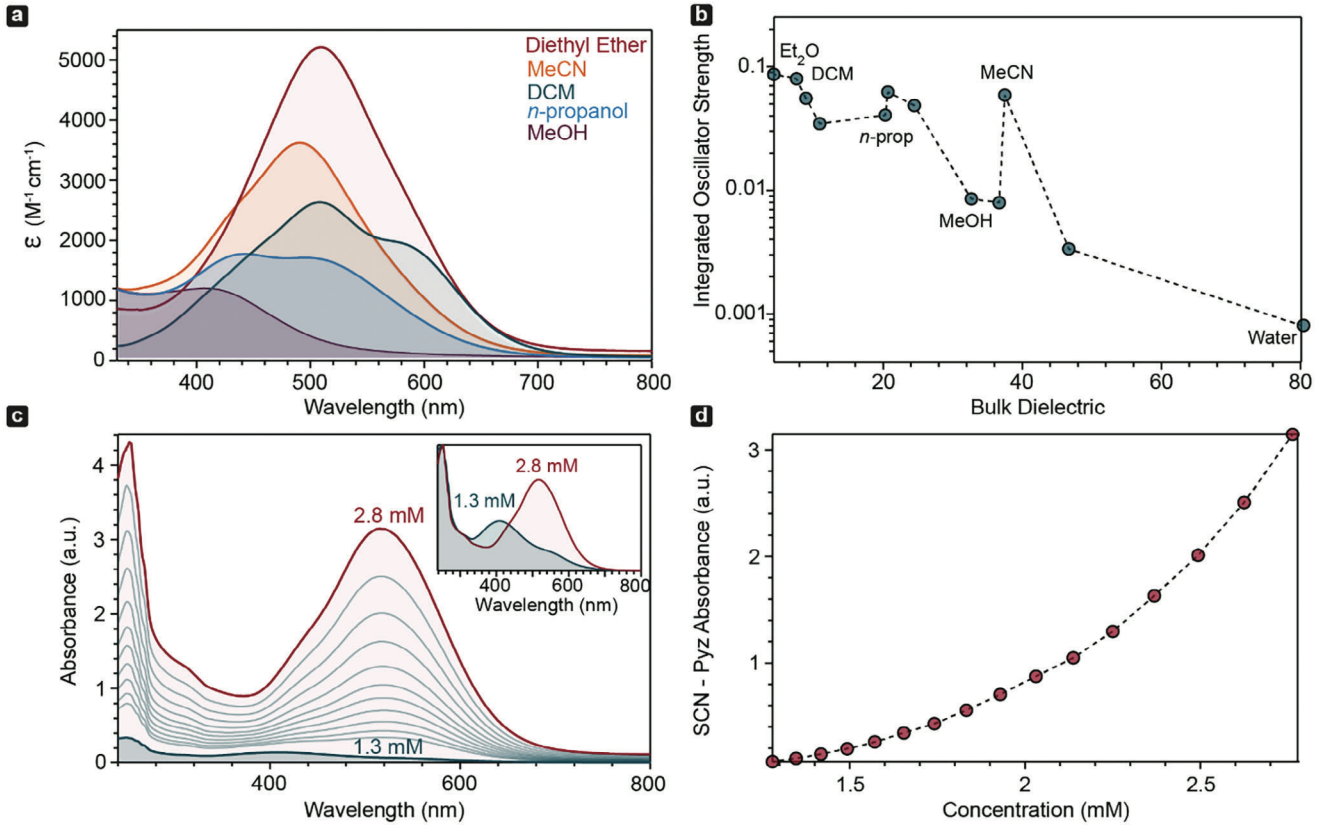

Figure 4. a) UV–vis spectrum of atmospherically oxidized Fe-SCN-pyz nanosheets suspended in diethyl ether, MeCN, DCM, n-propanol, and MeOH at 184 μM. b) Oscillator strength sum across the visible light bands vs solvent dielectric. c) Concentration dependence of atmospherically oxidized Fe-SCN-pyz nanosheets suspended in MeOH. d) Absorbance at ≈500nm as a function of concentration.

SCN^- and the closest N atom in pyrazine is shortened from 4.09 to 3.47 Å in the mixed-valent configuration. These results further suggest that upon 250 nm excitation during fluorescence, the excited electron-hole pair is localized on pyrazine. While some radiative decay is observed at ≈375 nm, given the close 3.47 Å proximity of the pendant SCN^-, the hole can transfer to the sulfur in SCN^-, forming the interlayer exciton that emits predominantly at ≈660 nm.

In summary, computations support the formation of interlayer excitons between pendant SCN- in one layer and pyrazine rings in the next layer during conditions, such as Fe oxidation and mixed valency, that place layers sufficiently close. These simulations agree with the experimental results in Figure 2: before iron oxidation, the solution-state UV–vis spectrum displays negligible absorbance in the visible region because interlayer interactions are disfavored and absorption bands only associated with isolated layers appear. However, upon iron oxidation, we observe the emergence of an intense, broad absorption band in the visible region consistent with the simulated UV–vis spectrum for interacting layers, where strong SCN-Fe^{3+} interactions favor interlayer excitonic coupling. The interlayer contraction predicted for strongly interacting layers is further supported experimentally by the PXRD pattern of these oxidized nanosheets that show with a distinct shift of the (001) reflection to lower d spacings.

Based on the hypothesis that the broad visible band arises from interlayer charge transfer, we explored the ability of solvent to screen the Coulombic electron-hole interactions. In the UV–vis response of the isostructural Co-SCN-pyz, authors attributed distinct solvatochromatic effects to the dielectric sensitivity of the pendant SCN^- group.[34] With the SCN^- group facilitating interlayer interactions and charge transfer we expected equally strong solvatochromic effects (**Figure** 4a).[34] Indeed, in low dielectric solvents (such as Et_2O, THF, and DCM) the interlayer charge transfer band is redshifted, intense, and broad. This result suggests that weaker solvent-SCN interactions strengthen interlayer interactions, facilitating interlayer charge transfer through increased aggregation and/or increased electron density on SCN^-. By contrast, high-dielectric solvents blueshift and weaken interlayer charge transfer, with the band nearly absent in solvents like MeOH. Strong solvent-SCN interactions weaken interlayer coupling and reduce interlayer charge transfer through weakening interlayer interaction and/or reducing electron density on NCS^-. While it is well known that the dielectric surrounding interlayer excitons has profound effects on its behavior, this phenomenon has only been explored in 2D heterostructures where insulative layers or organic layers are incorporated between strongly interacting materials to modulate the dielectric response.[45,56] In contrast, due to the solution processability and strong interlayer-induced aggregation, we report for the first time solvent effects on interlayer charge transfer excitons.

Given the evidence that the broadband feature arises from aggregation-induced charge transfer, we explored the effect of

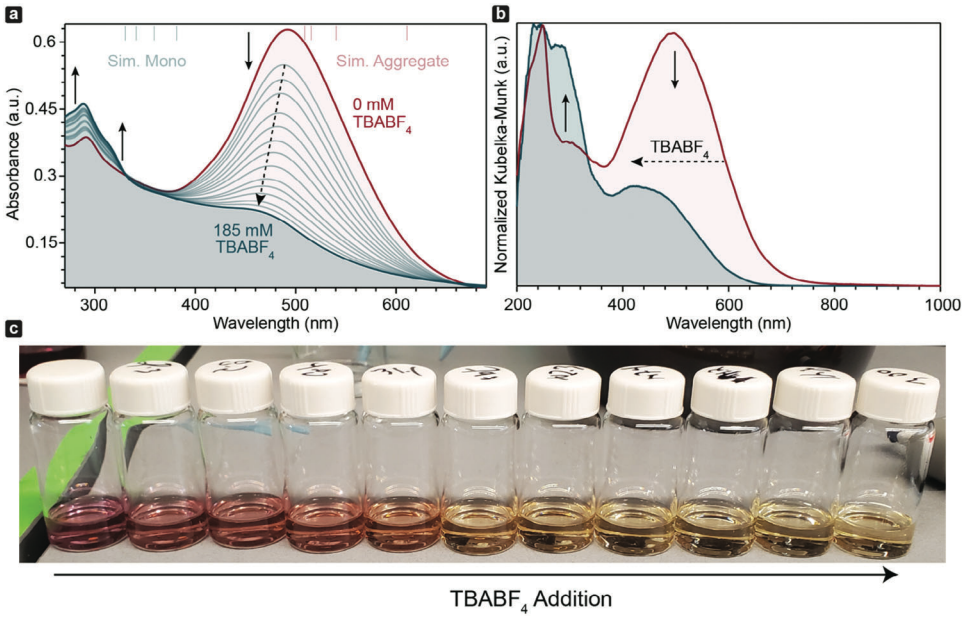

Figure 5. a) UV–vis spectrum of atmospherically oxidized Fe-SCN-pyz nanosheets suspended in MeCN as $TBABF_4$ is titrated in (tick marks at top of graph denote the most intense simulated absorptions for mixed valent aggregates and monolayers). b) DR UV–vis of air-oxidized Fe-SCN-pyz before and after saturating the pellet with a 1-M MeCN solution of $TBABF_4$. c) Photographic depiction of the solution upon addition of $TBABF_4$.

interlayer spatial distance. Accordingly, we expected non-linear deviations from Beer-Lambert's law at sufficiently high concentrations where sheets begin to aggregate.[57] Indeed, 184-µM methanolic suspensions shown in Figure 4a display only a weak band ≈400 nm attributable to the SCN − Fe^{3+} charge transfer. For sheets suspended at a far higher concentration of 2800 µM, the interlayer charge transfer band appears (Figure 4c). As shown in Figure 4d, intensity of the interlayer charge transfer band shows a non-linear concentration dependence at higher concentrations, suggesting aggregation-assisted charge transfer.

As an alternate route to controlling interlayer aggregation, we explored the ability of electrolytes to disrupt interlayer interactions. Molecular intercalation has been employed for interrupting interlayer interactions in black phosphorus and in 2D perovskite systems.[58,59] However, such intercalants have been limited to strongly interacting molecules that influence the electronic structure. **Figure 5a** shows the UV–vis spectrum of air-oxidized sheets suspended in MeCN with increasing equivalents of electronically inert $TBABF_4$. With greater quantities of electrolyte, the interlayer charge transfer blueshifts and decreases in intensity, while features associated with the simulated monolayer at ≈300 nm increase in intensity. The electrolyte ions stabilize the monolayers in solution and reduce interlayer interactions. As an additional synthetic handle for modulating the size of the intercalating anion, we explored anions of varying size. By adding the larger anion PF_6^- in the form of $TBAPF_6$ to a nanosheet suspension, a comparatively minor decrease in the interlayer charge transfer band appears (Figure S16, Supporting Information). We interpret this result to mean that the bulkier PF_6^- (254 pm compared to BF_4, 232 pm) proves less effective at intercalating between aggregates and screening charge. Conversely, addition of the smaller anion NO_3^- (179 pm) in the form of $TBANO_3$ causes the interlayer absorption band to vanish even with relatively few electrolyte equivalents (Figure S16, Supporting Information).

Finally, the synthetic tunability of Fe-SCN-pyz permits microscopic investigation into the structure-function nature of the interlayer charge transfer band. To tune the electronic nature of the donor orbitals, the analogous 2D material $Fe(Cl)_2(pyz)_2$ was synthesized. The successful synthesis was confirmed by PXRD (Figure S2, Supporting Information). Upon exposure to atmosphere and suspension in THF no visible broadband feature was observed (**Figure 6a**). However, a strong band ≈360 nm appears, which we assign to a Cl − Fe^{3+} charge transfer transition. In addition, DR UV–vis of the air-oxidized sample exhibits a broad band indicative of an IVCT in the NIR, like Fe-SCN-pyz, indicating a mixed-valent state (Figure S6, Supporting Information). These results provide further evidence of the orbital participation of SCN^- in the visible broadband feature. In a complementary fashion, we tuned the nature of the acceptor orbitals by synthesizing $Fe(SCN)_2$(4,4′-bipyridine)$_2$ (Figure S1, Supporting Information). Unlike Fe-Cl-py, upon atmospheric oxidation and suspension in THF, a purple color is observed. Figure 6b plots the corresponding solution-state UV–vis spectra, indicating that the interlayer NCS-4,4′–bipyridine charge transfer transition weakens and blueshifts relative to the NCS-pyz charge transfer band. We propose that this effect reflects the strong dependence of the interlayer charge transfer on molecular motion: the ability of 4,4′ bipyridine to rotate decreases favorable donor and acceptor orbital overlap.[60]

3. Conclusion

Here, we present a combined experimental-computational investigation into interlayer interactions of the van der Waals electroactive frameworks $Fe(SCN)_2$(pyrazine)$_2$. Although stable as

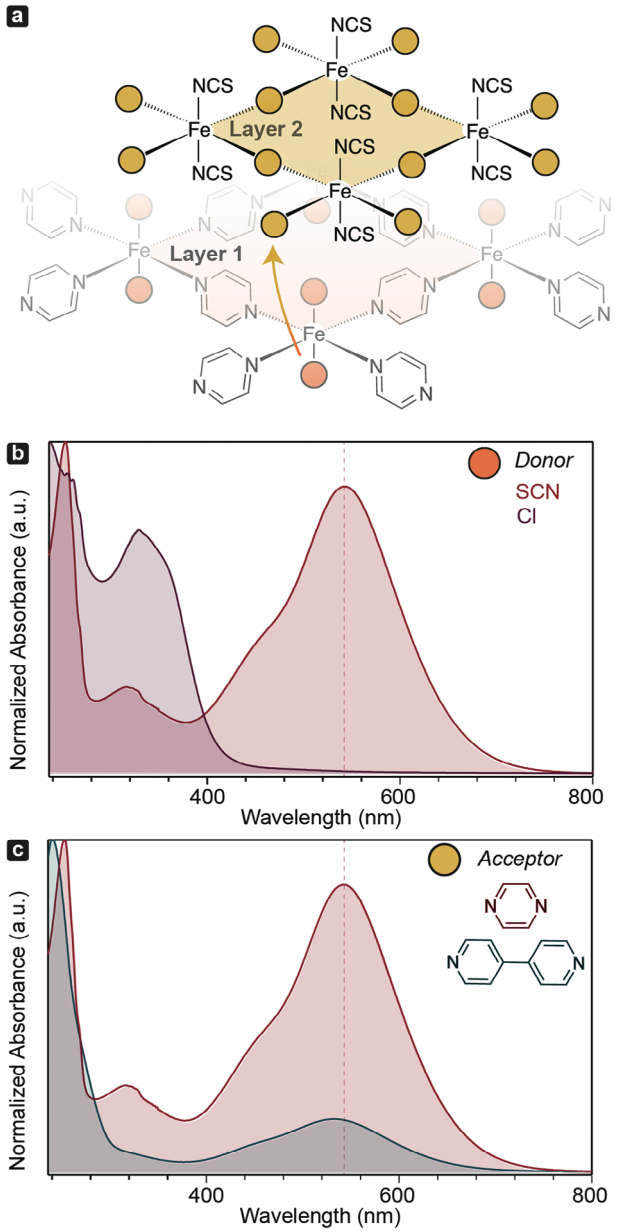

Figure 6. a) Representation of interlayer charge transfer process. b) UV–vis of atmospherically oxidized Fe-SCN-pyz, and Fe-Cl-pyz suspended in THF. c) UV–vis of atmospherically oxidized Fe-SCN-pyz and Fe-SCN-4,4'-Bipyridine suspended in THF.

isolated nanosheets when Fe^{2+}, partial oxidation induces strongly bound mixed valent aggregates that generate intense and broadband interlayer excitons with long lifetime photoluminescence. Due to the inherent tunability of the frameworks, we identified the origin of this charge transfer by systematically altering the composition of the organic and inorganic components. The SCN-to-pyrazine interlayer exciton can be modulated in intensity and peak position by tuning interlayer distance and electronic coupling strengths through changes in solvent, concentration, oxidation state, and electrolyte identity. Taken together, these results demonstrate the ability of molecular orbital interactions to dictate long-range behavior of topological materials.

4. Experimental Section

Materials: All commercial chemicals were used as received unless stated otherwise. Iron(II) sulfate heptahydrate (ACS grade, Fisher Chemical), iron(II) chloride (anhydrous, Strem), potassium thiocyanate (ACS grade, Fisher Chemical), potassium selenocyanate (99%, Thermo Scientific Chemicals), pyrazine (99%, Sigma Aldrich), 4,4′-Bipyridine (98%, Fisher Chemical), tetrabutylammonium hexafluorophosphate (recrystallized 3× from EtOH) (99%, Fisher Chemical), tetrabutylammonium tetrafluoroborate (recrystallized 3 × from MeOH/water mixtures) (99%, Fisher Chemical), tetrabutylammonium nitrate (98%, Fisher Scientific), ferrocenium tetrafluoroborate (technical grade, Sigma Aldrich), Diethyl ether (99%, Fisher Chemical), tetrahydrofuran (99.9%, Oakwood Chemical), N.N-Dimethylformamide (ACS grade, Fisher Chemical), dichloromethane (99.5%, Fisher Chemical), tert-butanol (99%, J.T. Baker), n-propanol (Macron Chemicals, 99%), acetone (99.5%, Fisher Chemical), ethanol ((200 proof, Decon Labs), methanol (99.8%, Fisher Chemical), Scientific) and nanopure water (Thermo Scientific, Barnstead Nanopure).

Characterization: Sample purity and crystallinity was verified by powder X-ray diffraction (PXRD) with a Bruker D2 Phaser benchtop diffractometer. Transmission electron microscope (TEM) images were collected with a FEI Tecnai by drop casting methanolic nanosheet/bulk suspensions onto carbon-coated copper TEM grids and drying naturally in air. Atomic force microscope (AFM) images were collected on a Bruker Dimension ICON with ScanAsyst by drop casting ethanolic nanosheet suspensions onto freshly piranha-cleaned Si/SiO_2 wafers, drying naturally under N_2. Solution-state UV–vis was collected on an Agilent Cary 5000 spectrophotometer and DR UV–vis-NIR was collected on the same instrument with a Harrick Scientific Praying Mantis Diffuse Reflection (DRP) accessory. Reflectance samples were diluted and the instrument was baselined with $BaSO_4$. Infrared Spectroscopy was collected with a Bruker Alpha II compact IR with an ATR attachment. Photoluminescence was collected with a HORIBA Fluoromax Spectrofluorometer and lifetime measurements were performed with a HORIBA TEMPro Time-Correlated Single Photon Counting Fluoroscence lifetime system.

^{57}Fe Mössbauer Spectroscopy: All samples were characterized by a SEE Co. ^{57}Fe Mössbauer spectrometer equipped with a Janis SVT-400 cryostat. The samples were prepared under an inert N_2 atmosphere by placing up to 30 mg of fine powder in a 14.5 mm Teflon cup with a Teflon plunger pressed into the cup to hold the sample. Data were collected until the signal-to-noise was deemed sufficient for meaningful analysis. This was dependent on the amount of sample loaded and the intensity of the source but was typically longer than 1 week. Samples were maintained under a nitrogen atmosphere for the duration of the experiment. Calibration of the instrument was performed using a standard iron sample provided by SEE Co. The data were analyzed using the Mössbauer spectral analysis software WMOSS4[61] written by Tom Kent and recently developed by Ion Prisecaru. The raw data were folded and calibrated using the iron standard supplied to us. The folded data were then fit to an appropriate model. We used two models to fit the data for this paper: the first is used for a pair of quadrupole doublets, and the second model is for a single quadrupole doublet. We used these models to refine the relevant parameters such as the shift of the quadrupole peak and the relative area of the peaks.

Chemical Oxidation of Fe-SCN-pyz with $FcBF_4$: Under an inert N_2 atmosphere, a ferrocenium tetrafluoroborate stock solution was prepared by dissolving 0.070 g of ferrocenium tetrafluoroborate in 15 mL of THF and left to stir for 2 h. Separately, under an inert N_2 atmosphere, 0.0318 g of Fe-SCN-pyz powder was exfoliated in 20 mL of MeOH via ultrasonication. To 4 separate vials, 4 mL of the Fe-SCN-pyz stock solution were added. While stirring, 112, 280, 560, and 896 µL of the ferrocenium

tetrafluoroborate stock solution was added to each vial, respectively (0.1 – 0.8 eq.). The solutions were left to stir for 48 h. The resulting solutions were dried down under dynamic vacuum and washed by ultrasonication with 10 mL of hexanes.

Spectroelectrochemistry of Suspensions of Fe-SCN-pyz: Under an inert N_2 atmosphere, 25 mg of Fe-SCN-pyz was exfoliated in 25 mL of MeOH via ultrasonication. 1 mL of this solution was added to a vial and dried under dynamic vacuum and resuspended in an 8-mL MeCN solution containing 310 mg of $TBAPF_6$ (recrystallized × 3 from EtOH). 4 mL of this solution was added to a quartz cuvette along with a 7 × 7 mm platinum mesh working electrode, a platinum wire counter electrode, and a silver pseudoreference electrode. Under an N_2 atmosphere, using a ThorLabs cuvette holder with multimode step index fiber optic patch cables connected to a Agilent Cary 5000 spectrophotometer, UV–vis spectra between 350 and 700 nm were collected every 2 min under an applied bias supplied by a GAMRY Instruments Interface 5000E potentiostat.

Photoluminescence of Suspended Air Oxidized Fe-SCN-pyz Nanosheets: A 150-µM solution of $Fe^{2+/3}$-SCN-pyz in 3 mL of dichloromethane was sparged for ≈15 min with N_2 to remove dissolved oxygen before it was loaded into an air-free quartz fluorometer cuvette and placed into a HORIBA Fluoromax Spectrofluorometer. The sample was excited with 250 nm light using a 5-nm slit width. Emission spectra were collected from 255 to 1000 nm using a 5 nm slit width. Spectra were corrected for instrumental features by subtracting a spectrum of neat dichloromethane. Lifetime measurements were performed on these same samples with a HORIBA TEMPro Time-Correlated Single Photon Counting Fluorescence lifetime system, NanoLED340 excitation source, and TBX picosecond detector. The excitation frequency was 25 kHz and the fluorescence decay was measured until 10 000 counts was reached. The resulting fluorescence curve was best fit with a χ^2 close to 1 with 3 exponentials.

Synthetic Procedures: *$Fe(SCN)_2(pyz)_2$ (Bulk)*. Following reported synthetic procedures,[33] 277.7 mg of $FeSO_4 \bullet 7H_2O$, 160 mg of pyrazine, and 194 mg of KSCN were dissolved in 5 mL of DI water, respectively. To a stirring solution of $FeSO_4$, the KSCN solution was drop-wise, followed by drop-wise addition of pyrazine. This mixture was allowed to stir for 24 h at RT. The resulting bright orange solid precipitate was washed with water (15 mL × 2), EtOH (15 mL × 1), and diethyl ether (15 mL × 1). The product was dried overnight at RT under dynamic vacuum.

$Fe(SCN)_2$(4,4′-Bipyridine)$_2$ (Bulk). Following reported synthetic procedures,[62,63] 277.7 mg of $FeSO_4 \bullet 7H_2O$, 306 mg of 4,4′-bipyridine, and 194 mg of KSCN were dissolved in 5 mL of DI water, respectively. While stirring the $FeSO_4$ solution the KSCN solution is added drop-wise, followed by drop-wise addition of 4,4′-bipyridine. The solution was allowed to stir for 24 h at RT. The resulting bright orange solid precipitate was washed with water (15 mL × 2), EtOH (15 mL × 1), and diethyl ether (15 mL × 1). The product was dried overnight at 120 °C under dynamic vacuum.

$Fe(Cl)_2(pyz)_2$ (Bulk). Following reported synthetic procedures,[64] 100 mg of anhydrous $FeCl_2$ and 705 mg of pyrazine were dissolved in 4 and 1 mL of EtOH, respectively. While stirring the $FeCl_2$ solution, the pyrazine solution was added drop-wise. The solution was allowed to stir for 24 h at RT. The resulting bright red solid precipitate was washed with EtOH (15 mL × 1), and diethyl ether (15 mL × 1). The product was dried overnight at RT under dynamic vacuum. A Rietveld refinement of the powder X-ray diffraction pattern was performed, using the known pattern from $Ni(Cl)_2(pyz)_2$, giving the simulated pattern shown in Figure S2, Supporting Information.[65]

$Fe(SCN)_2(pyz)_2$ (Nanosheets). Under N_2 5 mg of freshly prepared $Fe(SCN)_2(pyz)_2$ was suspended in 10 mL of deoxygenated MeOH. The solution was then sonicated in an ultrasonic bath (Branson 2510R-DTH Ultrasonic Cleaner) for 30 min. The resulting solution was centrifuged at 3000 RPM for 10 min to remove bulk material, and the remaining solution was dried under vacuum to yield nanosheets. Similar procedures were followed for $Fe(Cl)_2(pyz)_2$ and $Fe(SCN)_2$(4,4′-Bipyridine)$_2$ nanosheet generation.

Supporting Information

Supporting Information is available from the Wiley Online Library or from the author.

Acknowledgements

This material is based upon work supported by the Department of Energy through the Office of Basic Energy Sciences under Grant DE-SC0022147. C.H.H. acknowledges the support from the National Science Foundation under grant no. 2237345 and support from the Camille and Henry Dreyfus Foundation. D.C.J. acknowledges support from the National Science Foundation under grant no. DMR-2219512. C.K.B and C.H.H acknowledge the Research Corporation for Science Advancement (Cottrell Award). K.K. acknowledges the Japan Society for the Promotion of Science (JSPS) for an Overseas Research Fellowship (application number 202160772). This work made use of the CAMCOR facility of the Lorry I. Lowkey Laboratories at the University of Oregon.

Conflict of Interest

The authors declare no conflict of interest.

Data Availability Statement

The data that support the findings of this study are available from the corresponding author upon reasonable request.

Keywords

2D, exciton, metal-organic framework, van der Waals

Received: July 10, 2024
Revised: September 3, 2024
Published online:

[1] S. Wang, S. Zhao, X. Guo, G. Wang, *Adv. Energy Mater.* **2022**, *12*, 2100864.
[2] R. Rojaee, R. Shahbazian-Yassar, *ACS Nano* **2020**, *14*, 2628.
[3] W. Li, C. Liu, C. Gu, J. H. Choi, S. Wang, J. Jiang, *J. Am. Chem. Soc.* **2023**, *145*, 4774.
[4] P. Shen, P. Yin, Y. Zou, M. Li, N. Zhang, D. Tan, H. Zhao, Q. Li, R. Yang, B. Zou, B. Liu, *Adv. Mater.* **2023**, *35*, 2212172.
[5] A. Uri, S. C. de la Barrera, M. T. Randeria, D. Rodan-Legrain, T. Devakul, P. J. D. Crowley, N. Paul, K. Watanabe, T. Taniguchi, R. Lifshitz, L. Fu, R. C. Ashoori, P. S. Jarillo-Herrero, *Tunable Moiré QuasicrystalNature.* **2023**, *620*, 762.
[6] R. Niu, J. Li, W. Zhen, F. Xu, S. Weng, Z. Yue, X. Meng, J. Xia, N. Hao, C. Zhang, *J. Am. Chem. Soc.* **2024**, *146*, 1244.
[7] H. Wang, H. Wu, J. Zhang, Y. Liu, D. Chen, C. Pandey, J. Yin, D. Wei, N. Lei, S. Shi, H. Lu, P. Li, A. Fert, K. L. Wang, T. Nie, W. Zhao, *Nat. Commun.* **2023**, *14*, 5173.
[8] M. O. Sauer, A. Taghizadeh, U. Petralanda, M. Ovesen, K. S. Thygesen, T. Olsen, H. Cornean, T. G. Pedersen, *NPJ Comput. Mater.* **2023**, *9*, 35.
[9] J. Qiao, X. Kong, Z. X. Hu, F. Yang, W. Ji, *Nat. Commun.* **2014**, *5*, 4475.
[10] H. Liu, A. T. Neal, Z. Zhu, Z. Luo, X. Xu, D. Tománek, P. D. Ye, *ACS Nano* **2014**, *8*, 4033.
[11] J. Qiao, Y. Pan, F. Yang, C. Wang, Y. Chai, W. Ji, *Sci. Bull.* **2018**, *63*, 159.

[12] P. Sutter, H. P. Komsa, H. Lu, A. Gruverman, E. Sutter, *Nano Today* **2021**, *37*, 101082.
[13] Y. Zhao, J. Qiao, P. Yu, Z. Hu, Z. Lin, S. P. Lau, Z. Liu, W. Ji, Y. Chai, *Adv. Mater.* **2016**, *28*, 2399.
[14] Y. Sun, S. Luo, X. G. Zhao, K. Biswas, S. L. Li, L. Zhang, *Nanoscale* **2018**, *10*, 7991.
[15] M. Ricci, A. Ambrosetti, P. L. Silvestrelli, *J. Phys. Chem. C* **2020**, *124*, 27592.
[16] Z. Bian, J. Miao, Y. Zhao, Y. Chai, *Acc Mater Res* **2022**, *3*, 1220.
[17] A. Slassi, S. M. Gali, A. Pershin, A. Gali, J. Cornil, D. Beljonne, *J. Phys. Chem. Lett.* **2020**, *11*, 4503.
[18] Z. Dai, N. Lu, K. M. Liechti, R. Huang, *Curr. Opin. Solid State Mater. Sci.* **2020**, *24*, 100837.
[19] H. Kasai, K. Tolborg, M. Sist, J. Zhang, V. R. Hathwar, M. Ø. Filsø, S. Cenedese, K. Sugimoto, J. Overgaard, E. Nishibori, B. B. Iversen, *Nat Mater* **2018**, *17*, 249.
[20] A. J. Goodman, D. H. Lien, G. H. Ahn, L. L. Spiegel, M. Amani, A. P. Willard, A. Javey, W. A. Tisdale, *J. Phys. Chem. C* **2020**, *124*, 12175.
[21] S. Miao, T. Wang, X. Huang, D. Chen, Z. Lian, C. Wang, M. Blei, T. Taniguchi, K. Watanabe, S. Tongay, Z. Wang, D. Xiao, Y. T. Cui, S. F. Shi, *Nat. Commun.* **2021**, *12*, 3608.
[22] J. Qiao, X. Kong, Z. X. Hu, F. Yang, W. Ji, *Nat. Commun.* **2014**, *5*, 4475.
[23] Y. Liu, X. Duan, H. J. Shin, S. Park, Y. Huang, X. Duan, *Nature* **2021**, *591*, 43.
[24] G. Long, D. Maryenko, J. Shen, S. Xu, J. Hou, Z. Wu, W. K. Wong, T. Han, J. Lin, Y. Cai, R. Lortz, N. Wang, *Nano Lett.* **2016**, *16*, 7768.
[25] L. Viti, A. Politano, K. Zhang, M. S. Vitiello, *Nanoscale* **2019**, *11*, 1995.
[26] M. Huang, M. Wang, C. Chen, Z. Ma, X. Li, J. Han, Y. Wu, *Adv. Mater.* **2016**, *28*, 3481.
[27] H. Yu, G. B. Liu, J. Tang, X. Xu, W. M. E. Yao, *Sci. Adv.* **2017**, *3*, e1701696.
[28] K. F. Mak, J. Shan, *Nat. Nanotechnol.* **2018**, *13*, 974.
[29] Y. Lu, Y. Zhang, C. Y. Yang, S. Revuelta, H. Qi, C. Huang, W. Jin, Z. Li, V. Vega-Mayoral, Y. Liu, X. Huang, D. Pohl, M. Položij, S. Zhou, E. Cánovas, T. Heine, S. Fabiano, X. Feng, R. Dong, *Nat. Commun.* **2022**, *13*, 7240.
[30] J. H. Dou, M. Q. Arguilla, Y. Luo, J. Li, W. Zhang, L. Sun, J. L. Mancuso, L. Yang, T. Chen, L. R. Parent, G. Skorupskii, N. J. Libretto, C. Sun, M. C. Yang, P. V. Dip, E. J. Brignole, J. T. Miller, J. Kong, C. H. Hendon, J. Sun, M. Dincă, *Nat. Mater.* **2021**, *20*, 222.
[31] R. W. Day, D. K. Bediako, M. Rezaee, L. R. Parent, G. Skorupskii, M. Q. Arguilla, C. H. Hendon, I. Stassen, N. C. Gianneschi, P. Kim, M. Dincă, *ACS Cent. Sci.* **2019**, *5*, 1959.
[32] K. S. Pedersen, P. Perlepe, M. L. Aubrey, D. N. Woodruff, S. E. Reyes-Lillo, A. Reinholdt, L. Voigt, Z. Li, K. Borup, M. Rouzières, D. Samohvalov, F. Wilhelm, A. Rogalev, J. B. Neaton, J. R. Long, R. Clérac, *Nat. Chem.* **2018**, *10*, 1056.
[33] M. Wriedt, I. Jeß, C. Näther, *Eur. J. Inorg. Chem.* **2009**, *2009*, 1406.
[34] Y. H. Luo, C. Chen, C. He, Y. Y. Zhu, D. L. Hong, X. T. He, P. J. An, H. S. Wu, B. W. Sun, *ACS Appl. Mater. Interfaces* **2018**, *10*, 28860.
[35] S. Mahadevan, T. Liu, S. M. Pratik, Y. Li, H. Y. Ho, S. Ouyang, X. Lu, H. L. Yip, P. C. Y. Chow, J. L. Brédas, V. Coropceanu, S. K. So, S. W. Tsang, *Nat. Commun.* **2024**, *15*, 2393.
[36] A. E. Jailaubekov, A. P. Willard, J. R. Tritsch, W. L. Chan, N. Sai, R. Gearba, L. G. Kaake, K. J. Williams, K. Leung, P. J. Rossky, X. Y. Zhu, *Nat. Mater.* **2013**, *12*, 66.
[37] M. Feierabend, G. Berghäuser, A. Knorr, E. Malic, *Nat. Commun.* **2017**, *8*, 14776.
[38] S. Lukman, L. Ding, L. Xu, Y. Tao, A. C. Riis-Jensen, G. Zhang, Q. Y. S. Wu, M. Yang, S. Luo, C. Hsu, L. Yao, G. Liang, H. Lin, Y. W. Zhang, K. S. Thygesen, Q. J. Wang, Y. Feng, J. Teng, *Nat. Nanotechnol.* **2020**, *15*, 675.
[39] P. Rivera, J. R. Schaibley, A. M. Jones, J. S. Ross, S. Wu, G. Aivazian, P. Klement, K. Seyler, G. Clark, N. J. Ghimire, J. Yan, D. G. Mandrus, W. Yao, X. Xu, *Nat. Commun.* **2015**, *6*, 6242.
[40] M. A. Aly, M. Shah, L. M. Schneider, K. Kang, M. Koch, E. H. Yang, A. Rahimi-Iman, *Sci. Rep.* **2022**, *12*, 6939.
[41] X. Sun, Y. Zhu, H. Qin, B. Liu, Y. Tang, T. Lü, S. Rahman, T. Yildirim, Y. Lu, *Nature* **2022**, *610*, 478.
[42] J. Zhu, F. Shen, Z. Chen, F. Liu, S. Jin, D. Lei, J. Xu, *ACS Nano* **2024**, *18*, 13599.
[43] P. Nagler, G. Plechinger, M. V. Ballottin, A. Mitioglu, S. Meier, N. Paradiso, C. Strunk, A. Chernikov, P. C. M. Christianen, C. Schüller, T. Korn, *2D Mater.* **2017**, *4*, 025112.
[44] P. Nagler, M. V. Ballottin, A. A. Mitioglu, F. Mooshammer, N. Paradiso, C. Strunk, R. Huber, A. Chernikov, P. C. M. Christianen, C. Schüller, T. Korn, *Nat. Commun.* **2017**, *8*, 1551.
[45] Y. Jiang, S. Chen, W. Zheng, B. Zheng, A. Pan, *Light Sci Appl* **2021**, *10*, 72.
[46] C. Jiang, W. Xu, A. Rasmita, Z. Huang, K. Li, Q. Xiong, W. Gao, *Nat. Commun.* **2018**, *9*, 753.
[47] J. Liang, Q. Ai, X. Wen, X. Tang, T. Zhai, R. Xu, X. Zhang, Q. Fang, C. Nguyen, Y. Liu, H. Zhu, T. Terlier, G. P. Wiederrecht, P. M. Ajayan, X. Qian, J. Lou, *Mater. Today* **2024**, *74*, 77.
[48] C. Qian, M. Troue, J. Figueiredo, P. Soubelet, V. Villafañe, J. Beierlein, S. Klembt, A. V. Stier, S. Höfling, A. W. Holleitner, J. J. Finley, *Sci. Adv.* **2024**, *10*, eadk6359.
[49] Y. Huang, Y. H. Pan, R. Yang, L. H. Bao, L. Meng, H. L. Luo, Y. Q. Cai, G. D. Liu, W. J. Zhao, Z. Zhou, L. M. Wu, Z. L. Zhu, M. Huang, L. W. Liu, L. Liu, P. Cheng, K. H. Wu, S. B. Tian, C. Z. Gu, Y. G. Shi, Y. F. Guo, Z. G. Cheng, J. P. Hu, L. Zhao, G. H. Yang, E. Sutter, P. Sutter, Y. L. Wang, W. Ji, X. J. Zhou, et al., *Nat. Commun.* **2020**, *11*, 2453.
[50] W. Chen, G. Miceli, G. M. Rignanese, A. Pasquarello, *Phys. Rev. Mater.* **2018**, *2*, 073803.
[51] P. Liu, C. Franchini, M. Marsman, G. Kresse, *J. Phys. Condens. Matter* **2019**, *32*, 015502.
[52] T. Ketolainen, N. Macháčová, F. Karlický, *J. Chem. Theory Comput.* **2020**, *16*, 5876.
[53] F. D. Angelis, L. Armelao, *Phys. Chem. Chem. Phys.* **2010**, *13*, 467.
[54] M. Camarasa-Gómez, A. Ramasubramaniam, J. B. Neaton, L. Kronik, *Phys. Rev. Mater.* **2023**, *7*, 104001.
[55] C. Jamorski, M. E. Casida, D. R. Salahub, *J. Chem. Phys.* **1996**, *104*, 5134.
[56] J. Ji, J. H. Choi, *ACS Appl. Electron. Mater.* **2021**, *3*, 3052.
[57] Y. Liu, H. Liu, H. Yan, Y. Liu, J. Zhang, W. Shan, P. Lai, H. Li, L. Ren, Z. Li, L. Nie, *Adv. Sci.* **2019**, *6*, 1801615.
[58] C. Wang, Q. He, U. Halim, Y. Liu, E. Zhu, Z. Lin, H. Xiao, X. Duan, Z. Feng, R. Cheng, N. O. Weiss, G. Ye, Y. C. Huang, H. Wu, H. C. Cheng, I. Shakir, L. Liao, X. Chen, W. A. Goddard III, Y. Huang, X. Duan, *Nature* **2018**, *555*, 231.
[59] Y. Boeije, W. T. M. Van Gompel, Y. Zhang, P. Ghosh, S. J. Zelewski, A. Maufort, B. Roose, Z. Y. Ooi, R. Chowdhury, I. Devroey, S. Lenaers, A. Tew, L. Dai, K. Dey, H. Salway, R. H. Friend, H. Sirringhaus, L. Lutsen, D. Vanderzande, A. Rao, S. D. Stranks, *J. Am. Chem. Soc.* **2023**, *145*, 21330.
[60] C. Kallweit, G. Haberhauer, S. Woitschetzki, *Chem. Weinh. Bergstr. Ger.* **2014**, *20*, 6358.
[61] I. Prisecaru, W. 4. Mössbauer Spectral Analysis Software, (accssed: May 2023) http://www.wmoss.org/.

[62] C. J. Adams, J. A. Real, R. E. Waddington, *CrystEngComm* **2010**, *12*, 3547.
[63] M. Wriedt, S. Sellmer, C. Näther, *Dalton Trans.* **2009**, *38*, 7975.
[64] J. S. Haynes, J. R. Sams, R. C. Thompson, *Inorg. Chem.* **1986**, *25*, 3740.
[65] J. Liu, P. A. Goddard, J. Singleton, J. Brambleby, F. Foronda, J. S. Möller, Y. Kohama, S. Ghannadzadeh, A. Ardavan, S. J. Blundell, T. Lancaster, F. Xiao, R. C. Williams, F. L. Pratt, P. J. Baker, K. Wierschem, S. H. Lapidus, K. H. Stone, P. W. Stephens, J. Bendix, T. J. Woods, K. E. Carreiro, H. E. Tran, C. J. Villa, J. L. Manson, *Inorg. Chem.* **2016**, *55*, 3515.